International Journal of Nanomedicine

Dovepress
Taylor & Francis Group

Open Access Full Text Article

ORIGINAL RESEARCH

MOF-Ag Nanozyme for *Fusobacterium nucleatum* Eradication and Enhanced Nanocatalytic Therapy of Colorectal Cancer

Tan Wu[1,2,*], Xuejie Fei[2,*], Dan Xu[3,4,*], Qian Chen[2], Yang Zhang[1,5], Yuqin Jin[2], Yang Yang[2], Huanlong Qin[3,4], Fengzhou Du[6], Cheng Li[2]

[1]School of Pharmacy, Anhui Medical University, Hefei, 230032, People's Republic of China; [2]Department of Anesthesiology and Perioperative Medicine, Shanghai Key Laboratory of Anesthesiology and Brain Functional Modulation, Clinical Research Center for Anesthesiology and Perioperative Medicine, Translational Research Institute of Brain and Brain-Like Intelligence, Shanghai Fourth People's Hospital, School of Medicine, Tongji University, Shanghai, 200434, People's Republic of China; [3]Shanghai Clinical College, Anhui Medical University, Shanghai, 200072, People's Republic of China; [4]The Fifth Clinical Medical College, Anhui Medical University, Hefei, 230032, People's Republic of China; [5]Department of Pharmacy, Shanghai Eighth People's Hospital, Shanghai, 200235, People's Republic of China; [6]Department of Plastic and Reconstructive Surgery, Peking Union Medical College Hospital, Chinese Academy of Medical Sciences and Peking Union Medical College, Beijing, 100730, People's Republic of China

*These authors contributed equally to this work

Correspondence: Huanlong Qin; Yang Zhang, Email hlongqin@126.com; zhangyang0202@tongji.edu.cn

Purpose: This study aimed to develop a nanocatalytic-microbial therapeutic platform for colorectal cancer (CRC) that simultaneously eliminates the tumor-associated pathobiont *Fusobacterium nucleatum* (*F. nucleatum*) and enhances catalytic tumor therapy.

Methods: An iron-based metal-organic framework (NH_2-MIL-88B(Fe) composed of Fe^{3+} clusters and 2-aminoterephthalic acid, BDC-NH_2) loaded with silver nanoparticles (NH_2-MIL-88B(Fe)@Ag, denoted as MA) was constructed to integrate antibacterial activity with reactive oxygen species (ROS)-mediated tumor killing. The physicochemical properties, catalytic activity, and antibacterial performance of MA were characterized. Extracellular and intracellular ROS generation, cellular uptake, and cytotoxicity were evaluated in CRC cells. In vivo antitumor efficacy and biosafety were further assessed in a CT26 mouse colon cancer cells (CT26) subcutaneous tumor model with or without *F. nucleatum* inoculation.

Results: MA exhibited enhanced Fenton-like catalytic activity and generated more hydroxyl radicals than MOF alone in the presence of H_2O_2, indicating that Ag nanoparticles amplified ROS production. MA also showed potent antibacterial activity against *F. nucleatum*, enabling concurrent disruption of intratumoral bacteria and tumor cells. In vitro, MA induced pronounced ROS accumulation and significantly reduced CRC cell viability. In vivo, MA markedly suppressed tumor growth, with superior therapeutic efficacy in *F. nucleatum*-colonized tumors, demonstrating that bacterial elimination contributed substantially to tumor inhibition. No evident systemic toxicity was observed during treatment.

Conclusion: MA is a promising nanocatalytic platform for CRC therapy that combines direct antibacterial action against *F. nucleatum* with amplified ROS-mediated tumor cell killing. This dual-target strategy offers an effective and biocompatible approach for CRC treatment by integrating microbiota intervention with nanocatalytic therapy.

Keywords: colorectal cancer, *Fusobacterium nucleatum*, metal-organic framework, silver nanoparticles, nanozyme, nanocatalytic therapy

Introduction

Colorectal cancer (CRC) is a severe global health challenge. It is the second leading cause of cancer-related mortality and ranks third in incidence worldwide.[1,2] The complex connection between CRC pathogenesis and gut microbiome has garnered substantial scientific interest, revealing how microbial dysbiosis critically influences disease progression.[3–8] Among the various microbiota components, the gram-negative anaerobe, *F. nucleatum*, has emerged as a significant oncogenic pathogen. Notably enriched in the fecal samples of CRC patients, *F. nucleatum* correlates strongly with aggressive tumor phenotypes and unfavorable clinical outcomes.[9–11]

https://doi.org/10.2147/IJN.S603493
Received: 27 February 2026
Accepted: 29 April 2026
Published: 15 May 2026

The mechanistic underpinnings of *F. nucleatum* pathogenicity involve multiple molecular pathways. Through its unique FadA adhesin, *F. nucleatum* binds to E-cadherin on host cells, upregulates membrane-associated protein A1 expression, and initiates pro-tumorigenic signaling cascades. Additional mechanisms include adhesion via the RadD protein to CD147 receptors on CRC;[12] stimulation of intestinal epithelial nuclear factor kappa B (NF-κB) signaling mediated by Toll-like receptor 4 (TLR4);[13] and suppression of antitumor immunity, thereby diminishing the efficacy of immune checkpoint blockade therapy,[14] to their direct bacterial action, *F. nucleatum* metabolites significantly influence CRC biology. Butyrate shows promise in enhancing anti-PD-1 responses in colorectal cancer that is microsatellite-stable,[15] whereas succinic acid enhances tumor resistance to T cell-mediated killing by inhibiting the cGAS pathway, which is reversible with antibiotic treatment.[16] Collectively, these findings indicated that *F. nucleatum* is a promising therapeutic target for CRC management.

Existing antimicrobial strategies, particularly conventional antibiotics, have substantial limitations, including lack of specificity and potential for microbial resistance.[17–20] Consequently, innovative approaches for targeted bacterial eradication are urgently needed. Recent advances in nanotechnology offer compelling alternatives. We have developed antibacterial dendritic mesoporous silica and protein-based nanoparticles to eliminate intratumoral *F. nucleatum* and enhance CRC treatment efficacy.[21] Similarly, Chen et al engineered a nanomimetic system that selectively targeted tumor-colonizing bacteria, thereby overcoming immunosuppression and improving therapeutic outcomes.[22] These studies validated the feasibility and effectiveness of targeting *F. nucleatum* to augment CRC therapy.[23–25]

Nanocatalytic treatment has become a viable approach for transforming endogenous substrates into highly reactive species for targeted cancer ablation and antibacterial interventions.[26–29] Specifically, Fenton reactions that transform excess hydrogen peroxide (H_2O_2) in the tumor microenvironment into deadly hydroxyl radicals (•OH) can be triggered by iron-based nanocatalytic materials, thereby achieving confined oxidative damage to cancer cells with limited off-target effects.[30–34] Metal-organic frameworks (MOFs) are made up of organic linkers and metal ions and have attracted substantial attention as ideal nanocatalytic platforms owing to their high surface area, tunable porosity, and structural flexibility, which allows precise modulation of catalytic performance and multifunctional integration.[35–39] Beyond tumor therapy, MOF-based nanozymes have demonstrated potent antibacterial activity via redox-mediated bacterial membrane disruption and oxidative stress induction.[40–45] However, despite these advances, the interplay between intratumoral microorganisms and catalytic nanotherapy remains largely unknown. In colorectal cancer, where the microbial ecosystem, particularly *F. nucleatum*, plays a decisive role in tumor progression and therapeutic resistance, integrating microbial eradication with catalytic tumor therapy may unlock synergistic therapeutic benefits.

In this study, we designed a novel nanomedicine platform that integrates intratumoral *F. nucleatum* eradication with enhanced catalytic tumor therapy. We synthesized an iron-based MOF as a carrier and loaded silver nanoparticles onto its surface via a redox reaction to form a composite MA. This design leverages the Fenton reactivity of the MOF component to generate •OH from the tumor microenvironment H_2O_2, whereas the silver nanoparticles (Ag NPs) provide dual functionalities: direct antibacterial action against *F. nucleatum* and amplification of the Fenton reaction. Upon uptake by *F. nucleatum*-colonized colorectal cancer cells, MA simultaneously targets bacterial populations and tumor cells through the generation of synergistic ROS. This study established a practical and innovative strategy for improving CRC treatment by concurrently addressing oncogenic bacteria and enhancing catalytic tumor ablation (Scheme 1).

Methods

Materials and Reagents

Ferric (III) chloride hexahydrate, 2-aminoterephthalic acid and fluorescein isothiocyanate (FITC) were purchased form Aladdin. N,N-dimethylformamide (DMF) and acetic acid were purchased form macklin. Sodium borohydride was obtained from Yunnan Jingrui Technology Co., Ltd. Silver nitrate was obtained from China National Pharmaceutical Group Chemical Reagent Co., Ltd. Dulbecco's modified Eagle's medium (DMEM), Fetal bovine serum (FBS), penicillin −streptomycin and trypsin−EDTA (0.25%) were provided by Gibco. 4′,6-diamidino-2-phenylindole dihydrochloride (DAPI), Reactive Oxygen Species (ROS) Assay Kit, Calcein AM/PI Live/Dead Viability/Cytotoxicity Assay Kit and Annexin V-FITC Apoptosis Detection Kit were purchased from Beyotime. LIVE/DEAD Bacterial Staining Kit was

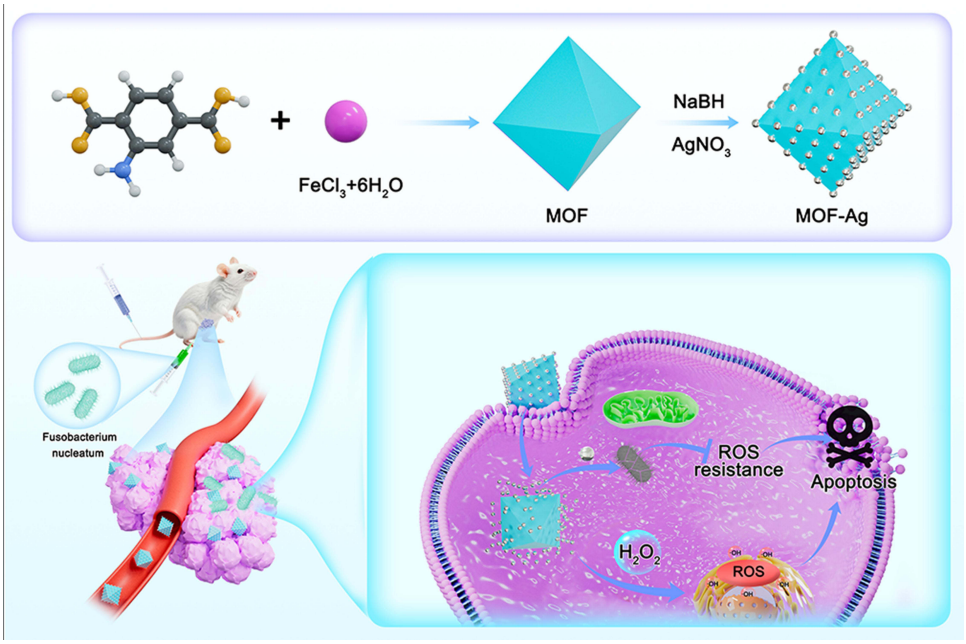

Scheme 1 Diagrammatic illustration of the MA synthesis process and its TME-activated cancer nanocatalytic therapy mechanism. The Fenton-like reaction of MA catalyzes H_2O_2 to produce •OH and inhibits tumor growth. Under the dual action of •OH and Ag, F. nucleatum-mediated tumor ROS resistance is weakened, and tumor cell apoptosis is expanded.

obtained from share-bio. Columbia Blood Agar Ready to Use Plate was purchased from BeNa Culture Collection. All the mice were maintained under specific pathogen free (SPF) conditions after purchasing from Sibeifu (Suzhou) Biotechnology Co., Ltd.

Synthesis of MOF

The synthesis of the NH_2-MIL-88B(Fe) (MOF) nanoparticles was based on a previous study. Briefly, 0.792 mL of acetic acid was added dropwise to the mixture after 0.504 g of 2-aminoterephthalic acid and 0.748 g of $FeCl_3 \cdot 6H_2O$ were combined in 60 mL of DMF and stirred until they were fully dissolved. The system was then placed in an oil bath at 120 °C and stirred for four hours. Once the mixture cooled to room temperature, it was washed once with DMF and twice with anhydrous ethanol to remove contaminants.

Synthesis of MA

A 4:1 mass ratio of the $AgNO_3$ solution was added to the MOF and stirred at 700 rpm for half an hour. Subsequently, sodium borohydride was added to ultrapure water, which was pre-cooled to 4 °C and continuously stirred for half an hour. After centrifugation, the MA was washed thrice with ultrapure water.

Characterization of MOF and MA

TEM was used to observe the morphologies of the MOF and MA. A Zetasizer Nanoseries (Malvern, UK) was used to assess DLS and Zeta potential. K-Alpha (Thermal Scientific) was used for XPS analysis. UV-2700i (Shimadzu, Japan) was used to record the UV–vis spectra of the nanoparticles. Inductively coupled plasma optical emission spectroscopy (ICP-OES, Agilent Technologies) was used to measure the concentration of iron ions in the MOF and MA nanoparticles.

Determination of Extracellular ROS Generation

To assess the capacity of NPs to produce ROS in vitro, we co-incubated MB with nanoparticles and observed the degradation of methylene blue to be degraded. Briefly, MB was incubated with different concentrations of MOF and MA

https://doi.org/10.2147/IJN.S603493

(50, 100, 200, 300, 400, and 500 μg/mL) for 10 min, with or without H_2O_2. The final concentrations of H_2O_2 and MB were 100 and 10 μg/mL, respectively. Subsequently, the changes in the absorbance of methylene blue at wavelengths of 400–800 nm using a UV spectrometer. Subsequently, DMPO was used to detect •OH radicals. Typically, DMPO is added to an MES buffer solution containing MOF and MA, followed by the addition or absence of H_2O_2. An electron paramagnetic resonance spectrometer was used to detect the •OH signal.

Cell Culture

CT26 cells purchased from the Chinese Academy of Sciences Shanghai Cell Bank were cultured in DMEM supplemented with 10% FBS and 1% streptomycin/penicillin at 37°C and 5% CO_2.

Cellular Uptake of MA

To prepare fluorescently labeled MA nanoparticles for cellular uptake studies, fluorescein isothiocyanate (FITC, Meilunbio) was conjugated to the amino groups of MOF within the MA nanocomposite. Briefly, 10 mg of MA nanoparticles were dispersed in 5 mL of anhydrous ethanol by sonication for 10 min. FITC (1 mg) was dissolved in 1 mL of dimethyl sulfoxide (DMSO) to obtain a 1 mg/mL solution. The FITC solution was then added dropwise to the MA dispersion under gentle stirring. The mixture was stirred at room temperature in the dark for 12 h to allow the reaction. The FITC-labeled MA nanoparticles (denoted as MA-FITC) were collected by centrifugation (11,000 rpm, 10 min) and washed three times with anhydrous ethanol followed by three times with deionized water to remove unreacted FITC. The final product was lyophilized and stored at 4 °C in the dark until further use.

CT26 cells were evenly spread on 12 well plates containing slides and incubated for 24 h. Next, MA nanoparticles grafted with Fluorescein Isothiocyanate (FITC) were diluted in DMEM and added to a 12 well plate. Slides were removed after incubation at different time points (0, 2, 4, 6, and 8 h). Observation of endocytosis of nanoparticles by cells using CLSM.

In vitro Cytotoxicity Assay

CT26 cells were seeded in 96-well plates for 24 h. This was followed by a 24-hour incubation period with different doses of MOF and MA (0, 5, 12.5, 25, 50, and 100 μg/mL). The cells were incubated for 40 min in DMEM containing 10% CCK-8 without serum. Absorbance was measured at 450 nm using a SpectraMax M3 microplate reader.

Determination of Intracellular ROS Generation

For 24 h, CT26 cells were seeded in a 96-well plate. The cells were then exposed to several formulations (PBS, MOF, and MA) at a concentration of 50 μg/mL for 24 h, with or without H_2O_2. Following a 25-minute dark incubation period at 37 °C with diluted DCFH-DA (Beyotime), intracellular ROS levels were measured using CLSM and flow cytometry.

Live/Dead Cell Staining Assay

For 24 h, the CT26 cells were seeded in a 12-well plate. The cells were treated with several formulations (PBS, MOF, and MA) with or without H_2O_2 for 24 h. The cells were incubated half-hour incubation with diluted Calcein AM/PI (Beyotime Biotechnology). After three PBS washes, cells were examined under a fluorescence microscope to check for cell death.

Cellular Apoptosis Detection

In a 12-well plate, CT26 cells were planted for 24 hours. The cells were then treated with several formulations (PBS, MOF, and MA) with or without H_2O_2 for 24 h. The cells were incubated for 30 min with diluted Calcein AM/PI (Beyotime Biotechnology). The cells were then washed thrice with PBS and examined under a fluorescence microscope to check for cell death.

Bacterial Culture

F. nucleatum was revived in a −80 °C freezer and added to brain heart infusion broth (BHI) medium before being transferred to an anaerobic chamber at 37 °C for cultivation.

In vivo Antibacterial Study

F. nucleatum 10^6 CFU/mL (1 mL) was incubated with different materials (PBS, H_2O_2, MOF, MOF + H_2O_2, MA, and MA + H_2O_2) for 24 h, followed by a continuous dilution of 103 times. The bacterial solution (100 μL) was coated on a blood agarose plate. After 24 h of cultivation in an anaerobic chamber at 37 °C, the antibacterial effect was evaluated using the plate-counting method. In addition, the survival status of the bacteria was determined using the NucGreen and EthD-III bacterial staining kits (Share-Bio). The two dyes were added under the above operating conditions and stained for 25 min before observation using CLSM.

In vivo Antitumor Study

Balb/c mice (female, 6 weeks, 20–25 g) were subcutaneously injected with CT26 cells (2×10^6) on the back of their right hind leg and randomly divided into five groups (n = 5): PBS (i.v)., 2) MOF (i.v)., 3) *Fn* (i.t). + MOF (i.v)., 4) MA (i.v)., and 5) *Fn* (i.t). + MA (i.v)., when the tumor size was between 50 and 100 mm^3, *F. nucleatum* was i.t. injected into tumor with the dose of 1×10^7 CFU.[22] Subsequently, treatment was administered via tail vein injection of nanomedicine on days 1, 3, and 5. Among them, i.t. represents intratumoral injection, and i.v. represents intravenous injection in mouse. The final administration concentration is based on the iron content, with an iron concentration of 31.8 μg/mL.[46] The nanoparticles in this study were measured by ICP, and the Fe content in MOF was 10%, while in MA it was 6.6%. Every two days, the body weight and tumor size of the mice were recorded. Tumor volume was calculated as 1/2 × ((tumor length) × (tumor width)^2). The tumor was removed on the fourteenth day. Paraformaldehyde and −80 °C were used to preserve the tumor tissue for staining.

Statistical Analysis

All experimental data are presented as mean ± standard deviation (SD). One-way analysis of variance (ANOVA) was used to analyze statistical significance. Statistical significance was indicated by * $p < 0.05$, ** $p < 0.01$, *** $p < 0.001$, and **** $p < 0.0001$. Data were analyzed using GraphPad software.

Results

Characterization of MOF and MA

To construct a platform capable of simultaneous antibacterial activity and catalytic tumor therapy, we developed a nanocomposite, denoted MA nanozyme, by embedding silver nanoparticles (Ag NPs) within an iron-based metal-organic framework (MOF). The successful synthesis and structural integration of the components were confirmed by transmission electron microscopy (TEM). As shown in Figure 1A. The MOF exhibits an irregular octahedral structure with a smooth surface. Following in situ reduction and loading of Ag, the resulting MA nanozyme (MA) composite maintained its structural integrity (Figure 1B). Crucially, the TEM images revealed the presence of small, dark-contrast points uniformly distributed throughout the MOF matrix, indicative of embedded Ag NPs. Elemental mapping analysis further confirmed the composition of the composite, clearly illustrating the spatial distributions of iron (Fe) from the MOF framework, nitrogen (N) and oxygen (O) originating from the organic linkers, and silver (Ag) (Figure 1C). We further characterized the optical properties, hydrodynamic size, and surface charge of the nanoparticles. The UV–Vis absorption spectroscopy (UV–Vis) absorption spectra showed distinct profiles for MOF and MA (Figure 1D). Dynamic light scattering (DLS) measurements indicated that the incorporation of Ag NPs resulted in a slight increase in the hydrodynamic diameter from 180.5 ± 2.1 nm for MOF to 191.6 ± 8.3 nm for MA (Figure 1E). The zeta potential also shifted from −7.14 ± 0.87 mV for MOF to −13.47 ± 0.45 mV for MA (Figure 1F), suggesting altered surface properties after Ag incorporation. X-ray photoelectron spectroscopy (XPS) was employed to analyze the elemental composition and chemical states of the materials (Figure S1). The high-resolution Fe 2p spectra of both the MOF and MA revealed that

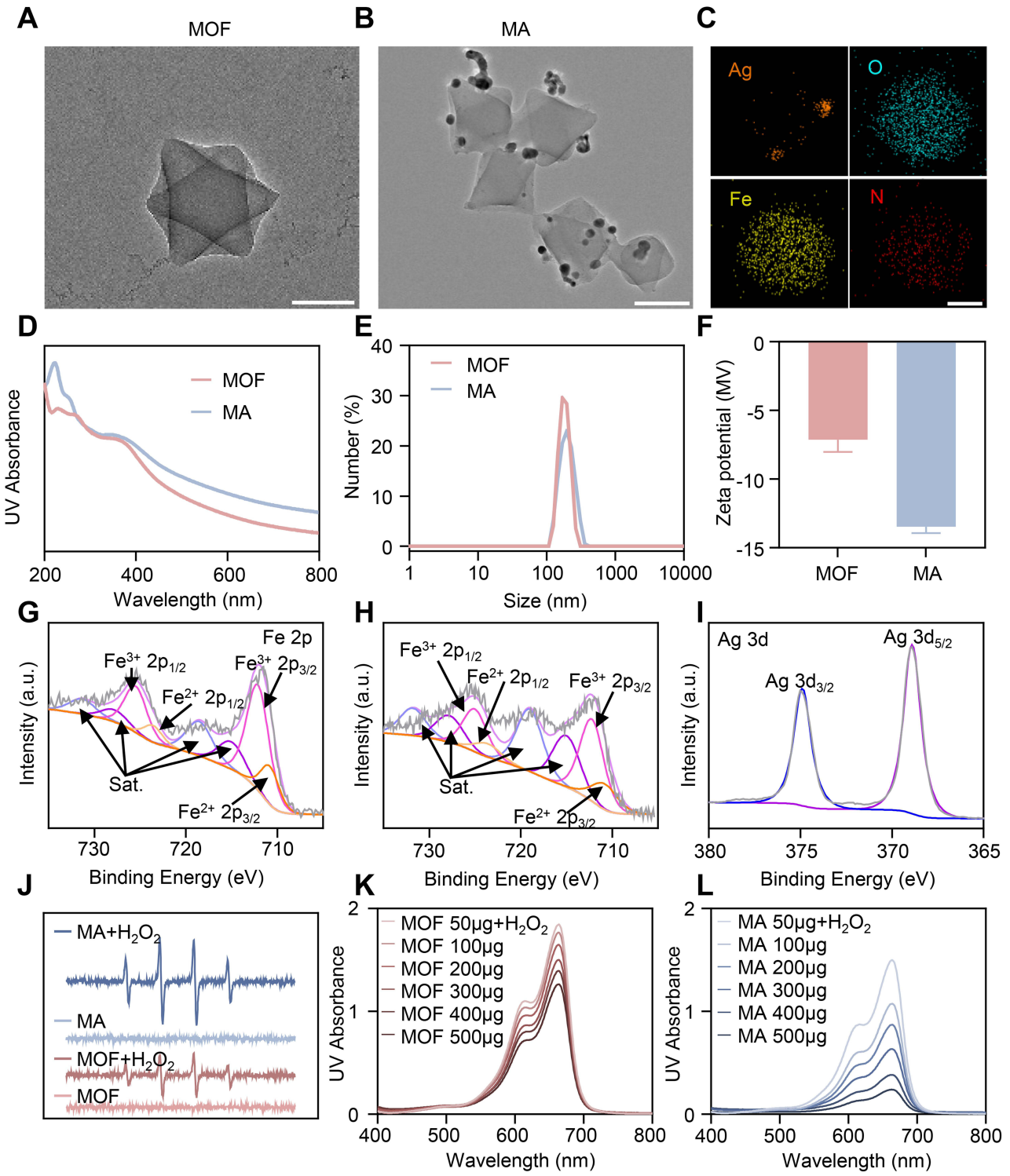

Figure 1 Characterization of MA nanozyme. TEM of (**A**) MOF and (**B**) MA. Scale bar: 100 nm. (**C**) Element mapping of MA. Scale bar: 50 nm. (**D**) UV–vis absorption spectra of MOF and MA. (**E**) DLS measurement of MOF and MA. (**F**) Zeta potential of MOF and MA measured using dynamic light scattering (n = 3). Fe 2p fine XPS spectra of (**G**) MOF and (**H**) MA. (**I**) Ag 3d fine XPS spectra of MA. (**J**) ESR spectra of DMPO for the •OH detection after different treatments. UV–vis absorption spectra of MB solution of (**K**) MOF and (**L**) MA in the presence of H_2O_2. Data were shown as mean ± SD (n = 3).

https://doi.org/10.2147/IJN.S603493

the proportion of Fe^{2+} increased from 23.26% in MOF to 25.45% in MA (Figure 1G and H). This enhancement in Fe^{2+} content is favorable for promoting the Fenton reaction. Additionally, the Ag 3d fine XPS spectrum confirmed that Ag existed predominantly in the metallic state (Figure 1I).

Extracellular ROS Generation by MOF and MA

To evaluate the •OH generation capability of MA in the presence of H_2O_2, electron paramagnetic resonance (EPR) spectroscopy was performed using 5,5-dimethylpyrroline-1-oxide (DMPO) as the spin-trapping agent. As shown in Figure 1J, both MOF and MA produced a characteristic 1:2:2:1 quartet signal corresponding to •OH after the addition of H_2O_2.[47] Notably, at the same mass concentration, the EPR signal intensity of MA was significantly stronger than that of MOF, indicating superior catalytic activity. Concentration-dependent EPR studies further demonstrated that •OH generation increased with nanoparticle concentration, confirming dose-response behavior (Figure S2). The •OH production was further corroborated using methylene blue (MB) as a reporter molecule, which decolorizes upon oxidation by •OH.[48] In the absence of H_2O_2, only a minor decrease in MB absorption was observed for both the MOF and MA (Figure S3). However, upon addition of H_2O_2, the MOF group showed a noticeable decrease in the MB absorption peak, and an even more drastic decrease, indicative of extensive •OH generation, was observed in the MA group (Figure 1K and L). Both EPR and MB decolorization assays consistently demonstrated that MA exhibited significantly enhanced catalytic efficiency compared to MOF alone, an effect likely attributable to the incorporation of Ag NPs.[49]

Cellular Uptake of MA by CT26 Cells

First, the cellular uptake of MA by the tumor cells was assessed. FITC-labeled MA was used to incubate CT26 mouse colon cancer cells, which were then examined by confocal laser scanning microscopy (CLSM) at different intervals. The results indicated the time-dependent cellular internalization of MA, supporting its potential for subsequent antitumor applications (Figure S4).

In vitro Cytotoxicity of MOF and MA Toward CT26 Cells

The cytotoxicity of the nanoparticles and their inhibitory effects on CT26 cells were assessed using a Cell Counting Kit-8 (CCK-8) assay. After incubation with varying concentrations of MOF or MA, the MOF group exhibited high biocompatibility with minimal cytotoxicity even at 100 μg/mL. MA, on the other hand, had somewhat higher cytotoxicity, which may be attributed to its higher catalytic activity (Figure S5). Given that the concentration of H_2O_2 in the tumor microenvironment was approximately 100 μM, we further evaluated the antitumor effect of the nanoparticles under these conditions. In the presence of 100 μM H_2O_2, MA induced significantly stronger tumor cell suppression than MOF, which is consistent with its enhanced •OH generation capability, as established in previous experiments (Figure S6).

Intracellular ROS Generation in CT26 Cells

To assess intracellular reactive oxygen species (ROS) generation, CT26 cells were treated with the different formulations and stained with 2,7-dichlorofluorescein diacetate (DCFH-DA). CLSM imaging revealed intense green fluorescence in the MA + H_2O_2 group, indicating substantial ROS production (Figure 2A). This result shows a pronounced rightward shift in the fluorescence intensity of MA in the presence of H_2O_2 (Figure 2B). Quantitative analysis of fluorescence intensity using FlowJo software further confirmed that MA induced significantly higher ROS levels than the control and MOF + H_2O_2 groups (Figure S7).

Live/Dead Cell Staining and Apoptosis Analysis of CT26 Cells

Using a live/dead cell labeling experiment, in which viable and dead cells were stained with calcein-AM and propidium iodide (PI), respectively, in vitro antitumor efficacy was further assessed. Fluorescence microscopy images showed weak green fluorescence and extensive red fluorescence in the MA + H_2O_2 group, indicating potent tumor cell death via the Fenton reaction (Figure 2E). Finally, Annexin V-FITC/PI labeling and flow cytometry were used to analyze apoptosis. The MA + H_2O_2 group exhibited markedly higher rates of both early and late apoptosis than the control and MOF + H_2O_2 groups (Figure 2C). Quantitative analysis further confirmed the enhanced proapoptotic effect of MA under H_2O_2-rich conditions (Figure 2D).

https://doi.org/10.2147/IJN.S603493

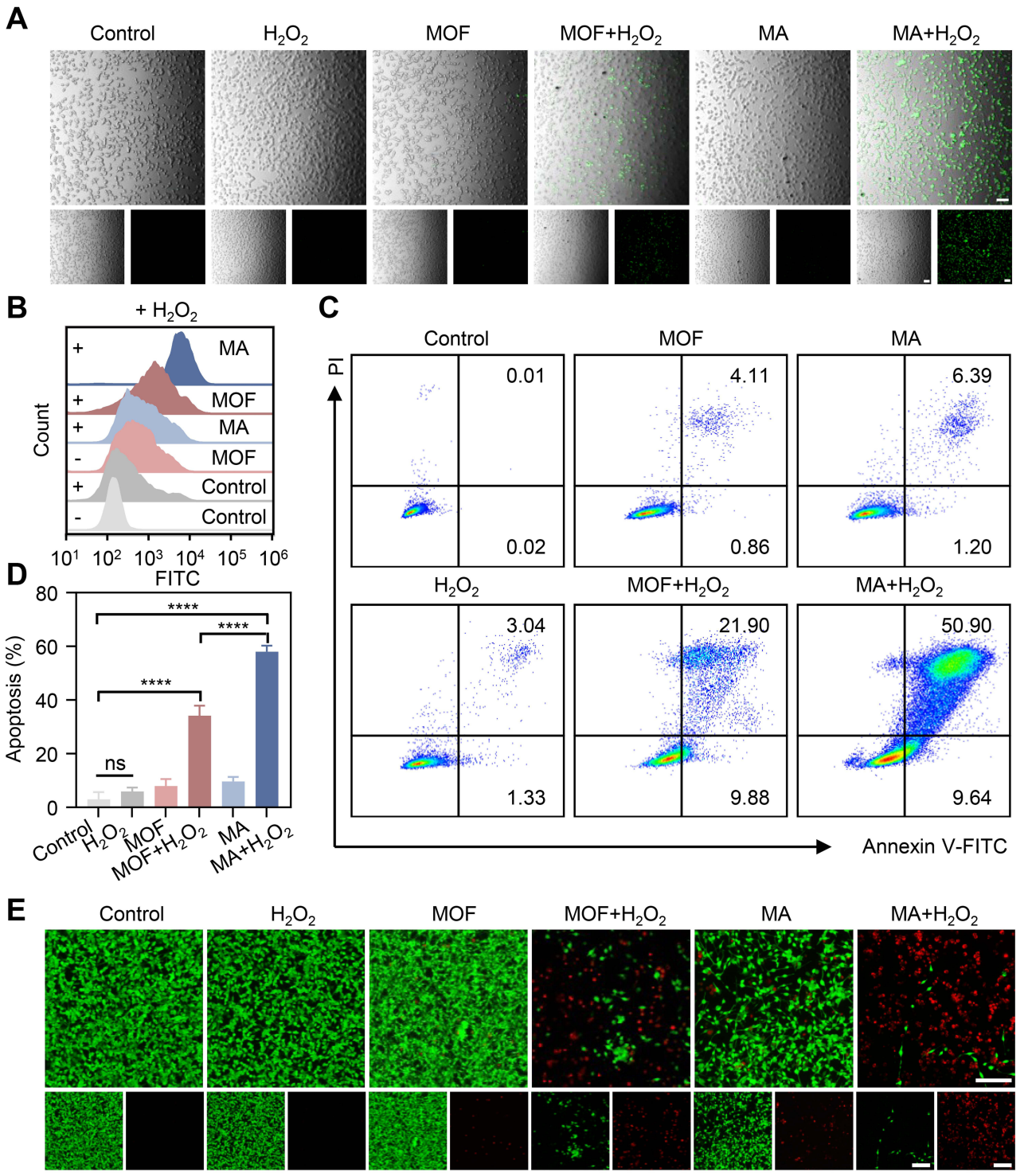

Figure 2 In vitro antitumor efficacy of MOF and MA with H_2O_2. (**A**) CLSM images of ROS level in CT26 cells in diverse treatment groups. Scale bar: 100 μm. (**B**) Analysis of ROS levels in CT26 cells using flow cytometry following different treatments. (**C**) Apoptosis analysis of CT26 cells treated with different nanoparticles using flow cytometry with Annexin V-FITC/PI assay. (**D**) Percentage of CT26 cells in diverse phases corresponding to panel. (**E**) Live/dead cell staining images of CT26 cells treated with different formulations with or without H_2O_2. Scale bar: 100 μm. Data were shown as mean ± SD (n = 3). ****P < 0.0001.

https://doi.org/10.2147/IJN.S603493

In vitro Antibacterial Activity of MA Against F. nucleatum

Given the crucial role of *Fusobacterium nucleatum* in promoting colorectal carcinogenesis, its elimination is a promising strategy for augmenting cancer therapies. Therefore, we evaluated the antibacterial activity of the nanoparticles against *F. nucleatum*. First, the bacteria were co-cultured with the various formulations for 24 h. The resulting bacterial solutions were collected, diluted, and plated on Columbia Blood Agar. Following a 24-hour anaerobic incubation at 37 °C, the bacterial colonies were enumerated. As shown in Figure 3A, whereas the PBS control group exhibited dense bacterial growth, treatment with MA alone led to a considerable reduction in colony-forming units (CFUs), emphasizing the intrinsic antibacterial ability of the (Ag NPs). The addition of H_2O_2 significantly increased the antibacterial activity. The MA + H_2O_2 group demonstrated the most effective clearance, with a substantial decrease in colony count compared with the other groups. This enhanced efficacy was attributed to the synergistic action of the Ag NPs and •OH generated via the Fenton reaction, leading to severe bacterial damage.

To further corroborate these findings, we assessed bacterial viability using a live/dead staining assay. Consistent with the colony counting results, CLSM images revealed that the MA-alone group showed a noticeable increase in dead bacteria compared to the control, MOF, and H_2O_2-only groups (Figure 3B). The MA + H_2O_2 group exhibited the most intense red fluorescence (dead bacteria) and the highest ratio of dead bacteria to live bacteria. Collectively, the results from both the quantitative plating and qualitative staining assays unequivocally demonstrate that MA, especially in combination with H_2O_2, possesses superior bactericidal activity against *F. nucleatum*. The effective eradication of a key oncogenic bacterium lays a solid foundation for exploiting this nanoplatform to promote tumor treatment.

In vivo Antitumor Efficacy and Biocompatibility of MA

Motivated by its strong antibacterial activity in vitro, we used a mouse model of colorectal cancer to assess MA's therapeutic potential of MA in vivo. First, *F. nucleatum*-associated colorectal cancer tumor models were randomly divided into five groups: 1) PBS (i.v)., 2) MOF (i.v)., 3) *Fn* (i.t). + MOF (i.v)., 4) MA (i.v)., and 5) *Fn* (i.t). + MA (i.v). Treatments were initiated the following day and administered intravenously every two days for a total of three doses

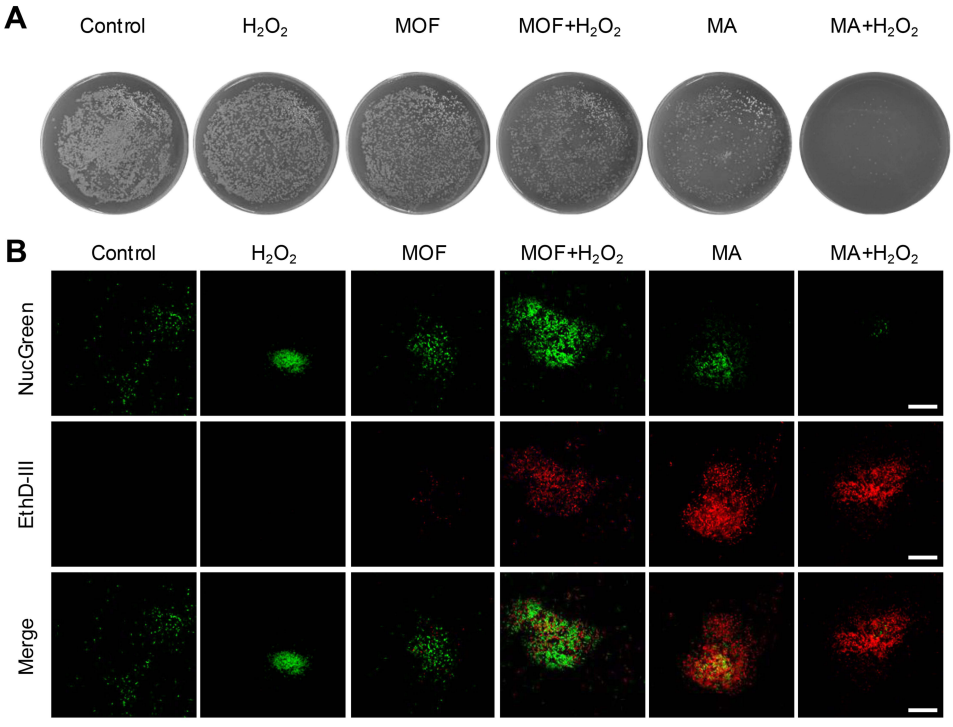

Figure 3 In vitro bactericidal performance assessment of MOF and MA against *F. nucleatum*. (**A**) Representative images of bacterial colonies on agar plates and the corresponding quantitative analysis of *F. nucleatum* treated with PBS, H_2O_2, MOF, MOF + H_2O_2, MA, and MA + H_2O_2. (**B**) Viability assessment of *F. nucleatum* treated with PBS, H_2O_2, MOF, MOF + H_2O_2, MA, and MA + H_2O_2 using Nucgreen and EthD-III staining. Scale bar: 50 μm.

https://doi.org/10.2147/IJN.S603493

(Figure 4A). Tumor volume and body weight were monitored throughout the study. Compared to the *Fn* + MOF group, the *Fn* + MA group had the strongest therapeutic impact, with the highest reduction in tumor growth resulting from the combination of MA's inherent anticancer action of MA and its capacity to target intratumoral *F. nucleatum*. This was evidenced by the smallest final tumor size (Figure 4B), most suppressed tumor growth curves (Figure 4C and F), and lowest excised tumor weights (Figure 4E). We postulate that this superior efficacy stems from a dual mechanism: MA not only directly kills tumor cells but also eliminates intratumoral *F. nucleatum*, thereby reversing *F. nucleatum*-mediated apoptosis resistance and alleviating its associated immunosuppression, while the released bacterial components from the killed *F. nucleatum* may potentially further stimulate an immune response. No discernible decrease in body weight was observed in any of the groups, suggesting that the therapies caused no systemic harm (Figure 4D). Hematoxylin and eosin (H&E) staining, immunohistochemistry, and fluorescence in situ hybridization (FISH) were used to gather and examine the tumor tissues (Figure 4G). H&E staining of the *Fn* + MA group revealed prominent features of cell death, including nuclear condensation and fragmentation. Immunohistochemical analysis for Ki67, a marker of cell proliferation, showed the weakest positive signal in the *Fn* + MA group, indicating effective suppression of tumor cell proliferation. Conversely, the TdT-mediated dUTP nick end labeling (TUNEL) assay, which detects DNA fragmentation during apoptosis, displayed the strongest signal in the *Fn* + MA group, confirming the induction of extensive apoptotic cell death. Furthermore, FISH using a universal bacterial probe confirmed the presence of *F. nucleatum* (red) in the inoculated groups and suggested its reduction following MA treatment, consistent with the designed antibacterial function. A semi-quantitative analysis was conducted on FISH images, and the results showed that the relative level of *F. nucleatum* in the MA group was lower, strongly indicating effective bacterial clearance (Figure S8). Besides, previous studies have established that FadA adhesin, a virulence factor secreted by *F. nucleatum*, binds to E-cadherin and activates the β-catenin signaling pathway. This activation further promotes the occurrence of tumors.[50] The results indicate that, the red fluorescence of the *Fn* + MOF group infected with *F. nucleatum* was significantly higher than that of the control group, attributed to the promotion of β-catenin expression by the presence of *F. nucleatum* (Figure S9). It is crucial that the treatment of the *Fn* + MA group reversed this change and significantly downregulated β-catenin. Overall, these findings suggest that MA nanoenzymes alleviate CRC cell proliferation and tumor progression by inhibiting the activation, clearance, and targeted blockade of key virulence interactions induced by *F. nucleatum* in the β-catenin pathway. In addition, the potential systemic toxicity of MA was further investigated by H&E staining of the major organs (heart, liver, spleen, lungs, and kidneys) collected from the treated mice. No significant histological abnormalities or inflammatory lesions were observed in any of the groups (Figure S10), confirming the biocompatibility of the MA nanozyme. These in vivo results demonstrated that MA possesses powerful antitumor efficacy, which is significantly enhanced in *F. nucleatum-infected* tumor microenvironments.

Discussion

The present study demonstrates that the rational integration of Ag nanoparticles into an iron-based MOF successfully generated a multifunctional nanozyme platform with both antibacterial and antitumor potential. In the characterization studies, TEM, elemental mapping, UV–vis spectroscopy, DLS, zeta potential, and XPS collectively confirmed the successful construction of MA while preserving the overall morphology of the parent MOF. Importantly, the increased Fe^{2+} proportion observed by XPS suggests that Ag incorporation not only introduced antibacterial functionality but may also modulate the redox environment of the MOF, thereby favoring Fenton or Fenton-like catalytic reactions. This structural basis is consistent with the enhanced catalytic behavior observed in subsequent assays.

In agreement with the extracellular ROS generation results, both EPR and MB degradation experiments confirmed that MA exhibited stronger ·OH generation capability than MOF in the presence of H_2O_2. This finding indicates that the incorporation of Ag improved the catalytic efficiency of the system, which may be attributed to altered electron transfer behavior and the increased availability of catalytically active Fe^{2+} sites. Since the tumor microenvironment contains endogenous H_2O_2, this enhanced ROS-generating capacity is particularly relevant for catalytic tumor therapy. At the same time, the stronger oxidative activity of MA also provides a mechanistic basis for its antibacterial action against *F. nucleatum*.

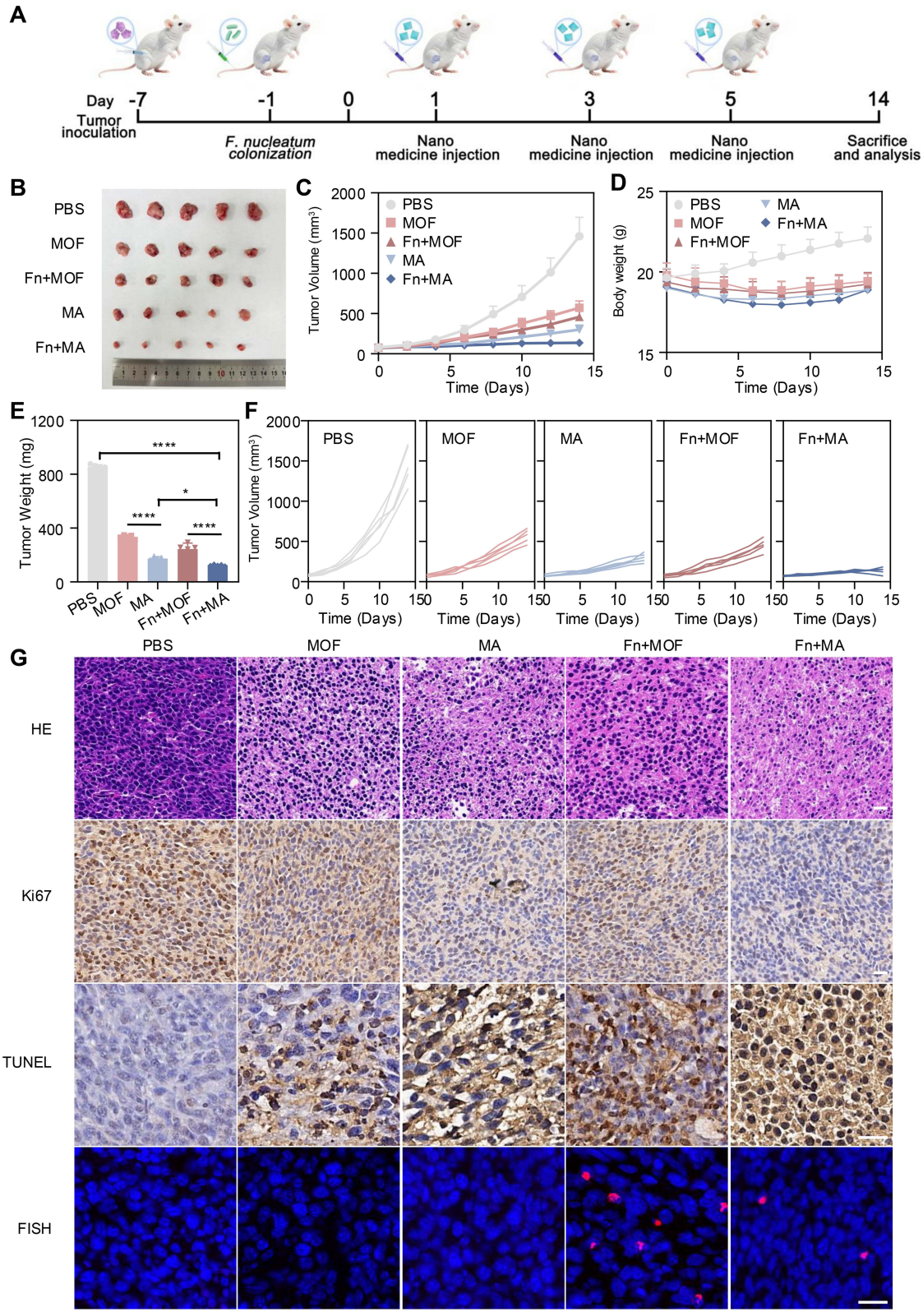

Figure 4 In vivo antitumor effects of MOF and MA. (**A**) Diagrammatic representation of the course of treatment in mice with CT26 tumors. (**B**) Representative excised tumor photograph images of different groups. (**C**) Tumor volume curves in different groups. (**D**) Body weight changes in different groups. (**E**) Weight of tumors in different groups. (**F**) Individual tumor growth curves of mice. (**G**) H&E, Ki67, TUNEL, and FISH to detect *F. nucleatum* infiltration (blue: DAPI-labeled nuclei, red: CY3 universal bacterial probe) staining images of tumor tissues after different treatments. Scale bar: 20 μm. Data were shown as mean ± SD (n = 3). *P < 0.05, ****P < 0.0001.

https://doi.org/10.2147/IJN.S603493

The cellular uptake experiment further showed that MA could be effectively internalized by CT26 cells in a time-dependent manner, which is an essential prerequisite for intracellular catalytic therapy. Efficient uptake likely facilitated the subsequent intracellular ROS generation and cytotoxic responses. Consistent with this, the in vitro cytotoxicity assays showed that MOF alone had relatively low toxicity, whereas MA exhibited stronger inhibitory effects on CT26 cells, especially in the presence of H_2O_2. This result suggests that the therapeutic activity of MA is not merely due to material exposure itself, but is closely associated with its catalytic activity under oxidative conditions.

The findings from intracellular ROS generation, live/dead staining, and apoptosis analysis further support this mechanism. MA, particularly when combined with H_2O_2, induced the highest ROS level in CT26 cells, which was accompanied by increased cell death and apoptosis. These results indicate that MA can effectively amplify oxidative stress in tumor cells and thereby trigger apoptotic pathways. The consistency among ROS, viability, and apoptosis data strengthens the conclusion that the antitumor effect of MA is largely driven by ROS-mediated catalytic therapy.

In the in vitro antibacterial study, MA showed clear bactericidal activity against *F. nucleatum*, and this effect was further enhanced in the presence of H_2O_2. Considering the established role of *F. nucleatum* in colorectal cancer progression, chemoresistance, and immune modulation, its elimination may provide benefits beyond simple antibacterial treatment. The strong antibacterial performance of MA is likely due to the combined effects of Ag-mediated bactericidal activity and ROS-induced oxidative damage. Therefore, MA may act not only as a tumor catalytic therapeutic agent but also as a regulator of the tumor-associated microbial microenvironment.

The in vivo antitumor study further demonstrated that MA achieved superior therapeutic efficacy in the *F. nucleatum*-associated tumor model, as evidenced by reduced tumor volume, lower tumor weight, decreased Ki67 staining, and increased TUNEL positivity. These findings suggest that the therapeutic advantage of MA may arise from a dual-action mechanism: direct oxidative killing of tumor cells and simultaneous elimination of tumor-promoting bacteria. This dual functionality is particularly meaningful in the context of colorectal cancer, where intratumoral bacteria can actively contribute to tumor progression and treatment resistance. In addition, the absence of obvious body weight loss or histological damage in major organs indicates favorable biocompatibility, supporting the translational promise of this nanozyme system.

Overall, this study highlights the value of integrating nanocatalytic therapy with antibacterial intervention for colorectal cancer treatment. By targeting both tumor cells and *F. nucleatum*, MA provides a synergistic strategy for remodeling the tumor microenvironment and enhancing therapeutic outcomes. Nevertheless, several limitations should be acknowledged. First, the precise molecular mechanisms by which MA modulates the interaction between bacterial clearance and tumor suppression require further investigation. Second, although the current in vivo results are encouraging, more comprehensive biosafety, pharmacokinetic, and biodistribution studies are still needed before clinical translation. Despite these limitations, the present work provides a promising foundation for the development of multifunctional nanozymes for microbiota-associated cancer therapy.

Conclusion

In conclusion, we developed a multifunctional Ag-integrated iron-based MOF nanozyme (MA) featuring both ROS-generating catalytic activity and antibacterial capability, which was specifically designed to target colorectal cancer together with its associated pathogenic microbiota. The key innovation of this work lies in the incorporation of Ag nanoparticles, which not only directly eliminate *F. nucleatum* but also enhance the catalytic performance of the Fe-based MOF, enabling a synergistic nanocatalytic-microbial therapeutic strategy. Experimentally, MA showed enhanced ROS generation, efficient cellular internalization, increased cytotoxicity and apoptosis in CT26 cells, and strong antibacterial activity against *F. nucleatum*. In vivo, MA exhibited superior antitumor efficacy in the CT26 colorectal cancer model, particularly in *F. nucleatum*-associated tumors, while showing no evident systemic toxicity. These findings demonstrate that simultaneous modulation of tumor cells and tumor-associated bacteria is an effective therapeutic approach and highlight the potential of this MOF-based platform for targeted treatment of microbiota-associated colorectal cancer.

Data Sharing Statement

Data supporting the findings of this study are available from the corresponding authors upon reasonable request.

Ethics Approval

All procedures involving animals are carried out in accordance with the "Guidelines for the Care and Use of Laboratory Animals" and ARRIVE guidelines, approved by the Ethics Committee of Tongji University (Ethics Approval Number: TJBH08425113). After the experiment, mice were euthanized using cervical dislocation method and the tumor was removed.

Acknowledgments

Correspondence: Cheng Li, Email li_cheng2017@163.com; Huanlong Qin, Email hlongqin@126.com; Yang Zhang, Email zhangyang0202@tongji.edu.cn. National Natural Science Foundation [grant number: 82271223], Shanghai Municipal Committee of Science and Technology for Program of Shanghai Academic/Technology Research Leader [grant number: 23XD1422900], Shanghai Municipal Health Commission [20244Z0007], Shanghai Rising-Star Program (24QB2706100), Hongkou District Health Commission [HKLCFC202405], Tongji University [2025-0674-YB-01] and Shanghai Fourth People's Hospital, School of Medicine, Tongji University [grant numbers: sykyqd01902, SY-XKZT-2023-1001, SY-YKYTS-2024-1002, sykyqd09501, SY-XKZI-2023-1009] for providing funding support to the current work.

Author Contributions

All authors made a significant contribution to the work reported, whether that is in the conception, study design, execution, acquisition of data, analysis and interpretation, or in all these areas; took part in drafting, revising or critically reviewing the article; gave final approval of the version to be published; have agreed on the journal to which the article has been submitted; and agree to be accountable for all aspects of the work.

Disclosure

The authors report no conflict of interest.

References

1. Siegel RL, Giaquinto AN, Jemal A. Cancer statistics, 2024. *CA Cancer J Clin*. 2024;74(1):12–49. doi:10.3322/caac.21820
2. Siegel RL, Miller KD, Wagle NS, Jemal A. Cancer statistics, 2023. *CA Cancer J Clin*. 2023;73(1):17–48. doi:10.3322/caac.21763
3. Cipe G, Idiz UO, Firat D, Bektasoglu H. Relationship between intestinal microbiota and colorectal cancer. *World J Gastrointest Oncol*. 2015;7(10):233–240. doi:10.4251/wjgo.v7.i10.233
4. Keku TO, Dulal S, Deveaux A, Jovov B, Han X. The gastrointestinal microbiota and colorectal cancer. *Am J Physiol Gastrointest Liver Physiol*. 2015;308(5):G351–63. doi:10.1152/ajpgi.00360.2012
5. Kim J, Lee HK. Potential role of the gut microbiome in colorectal cancer progression. *Front Immunol*. 2021;12:807648. doi:10.3389/fimmu.2021.807648
6. Qu R, Zhang Y, Ma Y, et al. Role of the gut microbiota and its metabolites in tumorigenesis or development of colorectal cancer. *Adv Sci*. 2023;10(23):e2205563. doi:10.1002/advs.202205563
7. Taddese R, Garza DR, Ruiter LN, et al. Growth rate alterations of human colorectal cancer cells by 157 gut bacteria. *Gut Microbes*. 2020;12(1):1–20. doi:10.1080/19490976.2020.1799733
8. Ternes D, Tsenkova M, Pozdeev VI, et al. The gut microbial metabolite formate exacerbates colorectal cancer progression. *Nat Metab*. 2022;4(4):458–475. doi:10.1038/s42255-022-00558-0
9. Liao Q, Zhou X, Wu L, et al. Gut microbial metabolite 4-hydroxybenzeneacetic acid drives colorectal cancer progression via accumulation of immunosuppressive PMN-MDSCs. *J Clin Invest*. 2025;135(11). doi:10.1172/JCI181243
10. Nobels A, van Marcke C, Jordan BF, Van Hul M, Cani PD. The gut microbiome and cancer: from tumorigenesis to therapy. *Nat Metab*. 2025;7(5):895–917. doi:10.1038/s42255-025-01287-w
11. Xu C, Fan L, Lin Y, et al. *Fusobacterium nucleatum* promotes colorectal cancer metastasis through miR-1322/CCL20 axis and M2 polarization. *Gut Microbes*. 2021;13(1):1980347. doi:10.1080/19490976.2021.1980347
12. Zhang L, Leng XX, Qi J, et al. The adhesin RadD enhances *Fusobacterium nucleatum* tumour colonization and colorectal carcinogenesis. *Nat Microbiol*. 2024;9(9):2292–2307. doi:10.1038/s41564-024-01784-w
13. Wang N, Fang JY. *Fusobacterium nucleatum*, a key pathogenic factor and microbial biomarker for colorectal cancer. *Trends Microbiol*. 2023;31(2):159–172. doi:10.1016/j.tim.2022.08.010
14. Pushalkar S, Hundeyin M, Daley D, et al. The pancreatic cancer microbiome promotes oncogenesis by induction of innate and adaptive immune suppression. *Cancer Discov*. 2018;8(4):403–416. doi:10.1158/2159-8290.CD-17-1134
15. Wang X, Fang Y, Liang W, et al. *Fusobacterium nucleatum* facilitates anti-PD-1 therapy in microsatellite stable colorectal cancer. *Cancer Cell*. 2024;42(10):1729–1746e8. doi:10.1016/j.ccell.2024.08.019
16. Jiang SS, Xie YL, Xiao XY, et al. *Fusobacterium nucleatum*-derived succinic acid induces tumor resistance to immunotherapy in colorectal cancer. *Cell Host Microbe*. 2023;31(5):781–797e9. doi:10.1016/j.chom.2023.04.010
17. Blair JM, Webber MA, Baylay AJ, Ogbolu DO, Piddock LJ. Molecular mechanisms of antibiotic resistance. *Nat Rev Microbiol*. 2015;13(1):42–51. doi:10.1038/nrmicro3380

18. Frieri M, Kumar K, Boutin A. Antibiotic resistance. *J Infect Public Health*. 2017;10(4):369–378. doi:10.1016/j.jiph.2016.08.007
19. MacGowan A, Macnaughton E. Antibiotic resistance. *Medicine*. 2017;45(10):622–628. doi:10.1016/j.mpmed.2017.07.006
20. Aminov RI. The role of antibiotics and antibiotic resistance in nature. *Environ Microbiol*. 2009;11(12):2970–2988. doi:10.1111/j.1462-2920.2009.01972.x
21. Chen Q, Zhu Y, Wang K, et al. Clearing intratumoral bacteria to augment tumor-therapeutic response by engineering antimicrobial dendritic mesoporous silica nanomedicine. *Nano Today*. 2023;52. doi:10.1016/j.nantod.2023.101994.
22. Chen L, Zhao R, Shen J, et al. Antibacterial *Fusobacterium nucleatum*-mimicking nanomedicine to selectively eliminate tumor-colonized bacteria and enhance immunotherapy against colorectal cancer. *Adv Mater*. 2023;35(45):e2306281. doi:10.1002/adma.202306281
23. Cui Y, Li B, He H, Zhou W, Chen B, Qian G. Metal-organic frameworks as platforms for functional materials. *Acc Chem Res*. 2016;49(3):483–493. doi:10.1021/acs.accounts.5b00530
24. Qu X, Yin F, Pei M, et al. Modulation of intratumoral *Fusobacterium nucleatum* to enhance sonodynamic therapy for colorectal cancer with reduced phototoxic skin injury. *ACS Nano*. 2023;17(12):11466–11480. doi:10.1021/acsnano.3c01308
25. Wang X, Chen Q, Zhu Y, et al. Destroying pathogen-tumor symbionts synergizing with catalytic therapy of colorectal cancer by biomimetic protein-supported single-atom nanozyme. *Signal Transduct Target Ther*. 2023;8(1):277. doi:10.1038/s41392-023-01491-8
26. Yang B, Chen Y, Shi J. Nanocatalytic medicine. *Adv Mater*. 2019;31(39):e1901778. doi:10.1002/adma.201901778
27. Huo CM, Ding PL, Tong SY, et al. Biomimetic nanozymes catalyze cascade reactions for enhanced tumor nanocatalytic therapy. *Nanoscale Horiz*. 2025;10(10):2381–2396. doi:10.1039/d5nh00110b
28. Jin Z, Jiang L, He Q. Critical learning from industrial catalysis for nanocatalytic medicine. *Nat Commun*. 2024;15(1):3857. doi:10.1038/s41467-024-48319-9
29. Zhao M, Zhang N, Yang R, Chen D, Zhao Y. Which is better for nanomedicines: nanocatalysts or single-atom catalysts? *Adv Healthc Mater*. 2021;10(8):e2001897. doi:10.1002/adhm.202001897
30. Zhang L, Li CX, Wan SS, Zhang XZ. Nanocatalyst-mediated chemodynamic tumor therapy. *Adv Healthc Mater*. 2022;11(2):e2101971. doi:10.1002/adhm.202101971
31. Han Y, Gao S, Zhang Y, et al. Metal-based nanocatalyst for combined cancer therapeutics. *Bioconjug Chem*. 2020;31(5):1247–1258. doi:10.1021/acs.bioconjchem.0c00194
32. Wang Y, Gao F, Li X, et al. Tumor microenvironment-responsive fenton nanocatalysts for intensified anticancer treatment. *J Nanobiotechnol*. 2022;20(1):69. doi:10.1186/s12951-022-01278-z
33. Qian X, Zhang J, Gu Z, Chen Y. Nanocatalysts-augmented Fenton chemical reaction for nanocatalytic tumor therapy. *Biomaterials*. 2019;211:1–13. doi:10.1016/j.biomaterials.2019.04.023
34. Liu C, Xu X, Chen Y, et al. Metabolism-regulating nanozyme system for advanced nanocatalytic cancer therapy. *Small*. 2024;20(24):e2307794. doi:10.1002/smll.202307794
35. Yang B, Ding L, Yao H, Chen Y, Shi J. A metal-organic framework (MOF) fenton nanoagent-enabled nanocatalytic cancer therapy in synergy with autophagy inhibition. *Adv Mater*. 2020;32(12):e1907152. doi:10.1002/adma.201907152
36. Yang B, Yao H, Yang J, Chen C, Shi J. Construction of a two-dimensional artificial antioxidase for nanocatalytic rheumatoid arthritis treatment. *Nat Commun*. 2022;13(1):1988. doi:10.1038/s41467-022-29735-1
37. Wang Q, Astruc D. State of the art and prospects in metal-organic framework (MOF)-based and MOF-derived nanocatalysis. *Chem Rev*. 2020;120(2):1438–1511. doi:10.1021/acs.chemrev.9b00223
38. Zhao D, Zhang W, Yu S, Xia SL, Liu YN, Yang GJ. Application of MOF-based nanotherapeutics in light-mediated cancer diagnosis and therapy. *J Nanobiotechnol*. 2022;20(1):421. doi:10.1186/s12951-022-01631-2
39. Gao S, Han Y, Fan M, et al. Metal-organic framework-based nanocatalytic medicine for chemodynamic therapy. *Sci China Mater*. 2020;63(12):2429–2434. doi:10.1007/s40843-020-1513-8
40. Pan X, Wu N, Tian S, et al. Inhalable MOF-derived nanoparticles for sonodynamic therapy of bacterial pneumonia. *Adv Funct Mater*. 2022;32(25). doi:10.1002/adfm.202112145
41. Cheng F, Yi X, Dai J, et al. Photothermal MXene@Zn-MOF-decorated bacterial cellulose-based hydrogel wound dressing for infectious wound healing. *Cell Rep Phy Sci*. 2023;4(10). doi:10.1016/j.xcrp.2023.101619
42. Chen H, Yu N, Wang J, et al. Construction of versatile fibroin/nanozyme hybrid microneedles with controllable phototherapeutic sterilization property against periodontitis. *Nano Today*. 2024;56. doi:10.1016/j.nantod.2024.102297.
43. Li J, Chu Z, Wang S, Liu H, Dong B. Study on synergistic mechanism of Cu-TCPP@MnO2 composites for photothermal/photodynamic/chemodynamic treatment of infected wound healing. *Chem Eng J*. 2025;512. doi:10.1016/j.cej.2025.162334.
44. Huang Y, Wan X, Su Q, et al. Ultrasound-activated piezo-hot carriers trigger tandem catalysis coordinating cuproptosis-like bacterial death against implant infections. *Nat Commun*. 2024;15(1):1643. doi:10.1038/s41467-024-45619-y
45. Xu C, Li J, Ou C, et al. Natural enzyme cascade bimetallic sulfide MoCuSx nanozyme for synergistic photothermal/photodynamic enhanced chemodynamic antimicrobial therapy of wound infection. *Chem Eng J*. 2024;499. doi:10.1016/j.cej.2024.156170.
46. Liu YJ, Dong SH, Hu WH, et al. A multifunctional biomimetic nanoplatform for image-guideded photothermal-ferroptotic synergistic osteosarcoma therapy. *Bioact Mater*. 2024;36:157–167. doi:10.1016/j.bioactmat.2024.02.007
47. Li L, Abe Y, Kanagawa K, et al. Distinguishing the 5,5-dimethyl-1-pyrroline N-oxide (DMPO)-OH radical quenching effect from the hydroxyl radical scavenging effect in the ESR spin-trapping method. *Anal Chim Acta*. 2004;512(1):121–124. doi:10.1016/j.aca.2004.02.020
48. Wiedmer D, Sagstuen E, Welch K, Haugen HJ, Tiainen H. Oxidative power of aqueous non-irradiated TiO 2 -H 2 O 2 suspensions: methylene blue degradation and the role of reactive oxygen species. *Appl Catal B*. 2016;198:9–15. doi:10.1016/j.apcatb.2016.05.036
49. Bhalla P, Rengaswamy R, Karunagaran D, Suraishkumar GK, Sahoo S. Metabolic modeling of host-microbe interactions for therapeutics in colorectal cancer. *NPJ Syst Biol Appl*. 2022;8(1):1. doi:10.1038/s41540-021-00210-9
50. Rubinstein MR, Wang X, Liu W, Hao Y, Cai G, Han YW. *Fusobacterium nucleatum* promotes colorectal carcinogenesis by modulating E-cadherin/beta-catenin signaling via its FadA adhesin. *Cell Host Microbe*. 2013;14(2):195–206. doi:10.1016/j.chom.2013.07.012